The Astrophysical Journal, 943:86 (10pp), 2023 February 1 https://doi.org/10.3847/1538-4357/acac22


# Multiple Populations in Low-mass Globular Clusters: Eridanus

Yue Wang[1], Baitian Tang[2,3], Chengyuan Li[2,3], Holger Baumgardt[4], Ricardo R. Muñoz[5], José G. Fernández-Trincado[6], Doug Geisler[7,8,9], and Yuanqing Fang[2]
[1] Key Laboratory of Optical Astronomy, National Astronomical Observatories, Chinese Academy of Sciences, Beijing 100101, People's Republic Of China
[2] School of Physics and Astronomy, Sun Yat-sen University, Zhuhai 519082, People's Republic Of China; tangbt@mail.sysu.edu.cn
[3] CSST Science Center for the Guangdong-Hong Kong-Macau Greater Bay Area, Zhuhai, 519082, People's Republic of China
[4] School of Mathematics and Physics, The University of Queensland, St Lucia, QLD 4072, Australia
[5] Departamento de Astronomia, Universidad de Chile, Camino del Observatorio 1515, Las Condes, Santiago, Chile
[6] Instituto de Astronomía, Universidad Católica del Norte, Avenida Angamos 0610, Antofagasta, Chile
[7] Departamento de Astronomia, Casilla 160-C, Universidad de Concepcion, Chile
[8] Instituto de Investigación Multidisciplinario en Ciencia y Tecnología, Universidad de La Serena, Avenida Raúl Bitrán S/N, La Serena, Chile
[9] Departamento de Astronomía, Facultad de Ciencias, Universidad de La Serena, Avenida Juan Cisternas 1200, La Serena, Chile
*Received 2022 May 7; revised 2022 December 14; accepted 2022 December 14; published 2023 January 27*

## Abstract

Multiple populations (MPs), characterized by variations in light elemental abundances, have been found in stellar clusters in the Milky Way, Magellanic Clouds, as well as several other dwarf galaxies. Based on a large number of observations, mass has been suggested to be a key parameter affecting the presence and appearance of MPs in stellar clusters. To further investigate the existence of MPs in low-mass clusters and explore the mass threshold for the formation of MPs, we carried out a project studying the composition of the stellar population in several low-mass Galactic globular clusters. Here we present our study on the cluster Eridanus. With blue-UV low-resolution spectra obtained with the OSIRIS/Multi-object spectrograph on the Gran Telescopio Canarias, we computed the spectral indices of CH and CN for a sample of giant stars and derived their carbon and nitrogen abundances using model spectra. A significant dispersion in the initial surface abundance of nitrogen was found in the sample, indicating the existence of MPs in Eridanus. Inspecting the age–initial mass distribution of in situ clusters with MPs, we find a slight trend that initial mass increases with increasing age, and the lowest initial masses of $\log M_{\rm initial} \sim 4.98$ and 5.26 are found at the young and old end, respectively, which might provide a rough reference for the mass threshold for clusters to form MPs. However, more observations of clusters with low initial masses are still necessary before any firm conclusion can be drawn.

*Unified Astronomy Thesaurus concepts:* Globular star clusters (656); Stellar abundances (1577)

## 1. Introduction

Variations in the chemical abundance in the light elements of globular clusters (GCs) were discovered half a century ago (Osborn 1971). Besides *normal* stars with chemical abundances similar to those of field stars, the stars showing chemical anomalies, e.g., deficiency in carbon, oxygen, and magnesium; enrichment in helium, nitrogen, sodium, and aluminum, were discovered to commonly exist in GCs as well in a series of observations, which are termed *multiple populations* (MPs) (e.g., Gratton et al. 2004; Carretta et al. 2010; Pancino et al. 2010, 2017; Masseron et al. 2019; Mészáros et al. 2020, and references therein). In addition to direct abundance analysis using spectra, photometry is also an effective way to study MPs, especially for faint clusters where high signal-to-noise ratio (S/N) spectra are unreachable. MP studies through photometry mainly use nitrogen-related molecular absorption bands in the UV-blue portion of the spectrum (e.g., NH, CN) (e.g., Piotto et al. 2012, 2015; Milone et al. 2017).

Although the existence of MPs is currently well accepted as a general feature of GCs, theoretical explanations for their origin have not reached a consensus (see Bastian & Lardo 2018, and references therein). Under the hypothesis of self-enrichment, which has been widely recognized, the ashes of high-temperature hydrogen burning were ejected from massive primordial stars and mixed with the interstellar medium. Then enriched stars that formed out of the mixture should show the enriched chemical pattern/chemical anomalies. The nature of the polluters has been debated for almost two decades, e.g., massive AGB stars (D'Ercole et al. 2010; Ventura & D'Antona 2011), fast-rotating massive stars (Decressin et al. 2007a, 2007b), supermassive stars (Denissenkov & Hartwick 2014; Denissenkov et al. 2015), massive interacting binaries (de Mink et al. 2009), and stellar mergers (Wang et al. 2020). However, none of the popular scenarios can reproduce the complex observed phenomena (Renzini et al. 2015; Bastian & Lardo 2018).

After the inspection of a large number of GCs, cluster mass, metallicity, and age were found to be the key parameters affecting the presence of MPs (Carretta et al. 2010; Bastian & Lardo 2018). To provide threshold parameters that can discriminate between and improve existing formation models, it is vital to investigate the detailed manifestation of MPs in critical conditions. For example, at the metal-rich end, NGC 6553 was found to be the most metal-rich GC with MPs, suggesting a potential metallicity ([Fe/H]) upper limit of −0.15 (Tang et al. 2017). In terms of cluster age, no clusters with ages younger than ∼2 Gyr have been found to host MPs so far, thus ∼2 Gyr seems to be the lower limit for the formation of MPs (Bastian & Lardo 2018, and references therein).

Cluster mass has been suggested to be a universal parameter that determines the complexity of MPs, e.g., more massive clusters have larger variations in abundance and fractions of enriched populations (Bastian & Lardo 2018; Milone et al. 2020); more massive Type II GCs show larger iron spread (Milone & Marino 2022). Exploring the critical cluster mass for the formation of MPs will certainly expand upon the current MP scenarios. The possible mass boundary ($\sim 5 \times 10^4 M_\odot$) proposed in Li et al. (2019) seems to well separate the intermediate-age GCs (2–10 Gyr) with and without MPs. But the situation is more complicated for older GCs. In this respect, NGC 6535 (mass $= 2.2 \times 10^4\, M_\odot$) was suspected to be the lowest-mass GC to harbor MPs based on high-resolution spectroscopy (Bragaglia et al. 2017); moreover, MPs were found to probably exist in the lower-mass GC ESO452-SC11 (mass $\sim (6.8 \pm 3.4) \times 10^3\, M_\odot$) with low-resolution spectra (Simpson et al. 2017). Palomar 13 (Pal 13) was recently found to show MPs based on low-resolution spectra (Tang et al. 2021), and it could probably be the lowest-mass GC (mass $\sim 10^{3.5}\, M_\odot$, our most up-to-date estimation) with MPs.

Under the hypothesis of self-enrichment, a minimum mass is indeed required by a cluster to retain ejecta from an initial generation and allow the formation of a subsequent generation, depending of course on the velocity of the ejecta. For example, from hydrodynamical simulations, Vesperini et al. (2010) and Bekki (2011) both found a lower-mass limit, $\sim 10^{4.8}$–$10^5\, M_\odot$ and $\sim 10^6\, M_\odot$, respectively, for stellar clusters to retain enough ejecta of primordial generation stars and form an enriched generation of stars. At the same time, the mass threshold has also been suggested by observations. Based on the Na–O anticorrelations, Carretta et al. (2010) showed that a minimum present-day mass of a few tens of thousands of solar mass was required for stellar clusters to present MPs. Charlie & Spergel (2011) found that in the Large Magellanic Cloud (LMC) only clusters more massive than about $10^4\, M_\odot$ showed MPs, and this critical mass was also consistent with their model prediction of the mass at which ram pressure was sufficient to remove the gas within the cluster. Moreover, Milone et al. (2020) suggested a threshold of $\sim 1.5 \times 10^5\, M_\odot$ in initial mass for Galactic GCs to form MPs, while clusters in the Magellanic Clouds seemed not to follow this limit.

Although several papers have proposed possible mass thresholds for stellar clusters to form MPs based on observations as mentioned above, no final conclusion can be derived until we have a comprehensive understanding of the composition of the stellar populations of low-mass clusters. However, this is challenging work since low-mass clusters have few bright giant stars and are often located at large distances from the Sun. To take the study one step further and have a better understanding of the existence of MPs at the low-mass end, we have observed several low-mass Galactic GCs. Since they are remote objects, low-resolution spectra of their member stars were obtained to ensure enough S/N to derive the abundances of relevant species. As a subsequent work of our last study of MPs in Pal 13 (Tang et al. 2021), here we present the first study of the composition of the stellar population in the GC Eridanus, which has a present-day mass of $1.16 \times 10^4\, M_\odot$ (Baumgardt et al. 2019).

Eridanus was first discovered by Cesarsky et al. (1977). Having a metallicity of about [Fe/H] $= -1.4$ and a distance of about 90 kpc (e.g., Harris 1996, 2010 edition; see Section 3.1 for details), Eridanus is one of the most metal-rich clusters in the outer halo. With an age of 10.5 Gyr, it is also younger compared with inner-halo GCs at similar metallicities (Beccari et al. 2012). Hence, Eridanus is expected to have an external origin. Although being an interesting object for studies, it has not been explored spectroscopically, nor have its MP properties, due to its large Galactocentric distance. In this paper, we analyze the low-resolution spectra of Eridanus member stars to estimate their carbon and nitrogen abundances, searching for possible abundance variations that indicate MPs. In Section 2, we outline the observations and spectral reduction briefly. In Section 3, we analyze the spectra of member stars carefully and show our major results. A discussion and summary are given in Sections 4 and 5, respectively.

**Table 1**
Observation Details

| Observing Block | Date | Exposure Time (s) | Air Mass | Seeing (″) |
|---|---|---|---|---|
| OB02 | 2018-12-8 | 1800 × 2 | 1.70 | 1.2 |
| OB06 | 2018-12-8 | 1800 × 2 | 1.55 | 1.1 |
| OB07 | 2018-12-8 | 1580 × 2 | 1.58 | 1.0 |
| OB09 | 2018-12-10 | 1800 × 2 | 1.55 | 1.2 |
| OB10 | 2018-12-10 | 1800 × 2 | 1.62 | 1.2 |

## 2. Observation and Data Reduction

### 2.1. Observation

The observations were carried out using the OSIRIS/Multi-object spectrograph (MOS)[10] mounted on the Gran Telescopio Canarias (GTC), Observatorio del Roque de los Muchachos, under program No. GTC2-18BCNT in 2018 December. The sample of stars for observation was initially selected from the Gaia DR1 catalog (Gaia Collaboration et al. 2016) by coordinates within the region of Eridanus GC. Given that the slitlet observation forbids two targets from overlapping in the dispersion direction and brighter targets generate higher S/N spectra within a given time, 19 member stars were finally observed (Section 3). The observation consists of five observing blocks (OBs) with a total exposure time of 4.88 hr (see Table 1). Using R2500U as the dispersion element, the obtained spectra cover the wavelength range of 3500 −4600 Å with a nominal spectral resolution of ∼2500.

### 2.2. Data Reduction

The data reduction was conducted following the procedure described in Tang et al. (2021), which can be summarized briefly as follows. The GTCMOS pipeline[11] was first used to complete basic steps: for each OB, the observed spectral images were bias subtracted, combined, wavelength calibrated, flat-field corrected, and extracted to multiple one-dimensional spectra. After velocity correction, the observed spectra were calibrated using model spectra in order to minimize the uncertainty caused by the flat-field correction. Considering the stellar parameters estimated in Section 3, we generated the model spectra with iSpec[12] (Blanco-Cuaresma et al. 2014; Blanco-Cuaresma 2019), where the SPECTRUM radiative transfer code and line list, MARCS model atmospheres

[10] http://www.gtc.iac.es/instruments/osiris/osiris.php
[11] https://www.inaoep.mx/~ydm/gtcmos/gtcmos.html
[12] https://www.blancocuaresma.com/s/iSpec

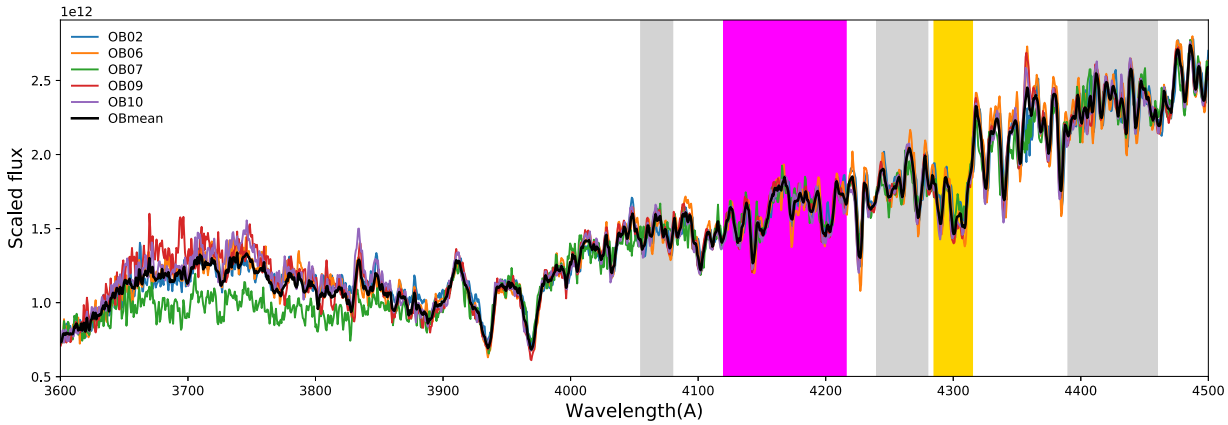


**Figure 1.** Example of calibrated spectra of five OBs and the co-added one. The gray regions indicate the pseudo-continuum, while the red and yellow regions indicate the feature wavelengths for measuring the spectral indices of CN4142 and CH4300, respectively.

(Gustafsson et al. 2008) and the solar abundances from Asplund et al. (2005) were adopted. After the calibration, the spectra of the five OBs were co-added for each star (Figure 1).

## 3. Analysis and Results

### 3.1. Basic Information on the Sample of Stars

We updated the Gaia photometry with Gaia DR2 data, and extinctions in the $G$, $BP$, and RP bands were computed using the coefficients provided by the team (Gaia Collaboration et al. 2018). We also cross-matched the sample stars with the catalog of Muñoz et al. (2018) to obtain their $g$ and $r$ band magnitudes. For the two stars (eri08 and eri10) that were not matched, we supplemented their $g$ and $r$ band magnitudes by transforming them from the Gaia photometry with the photometric relations provided in the Gaia Data Release 2 Documentation release 1.2.[13] The systematic differences between the magnitudes of Muñoz et al. (2018) and those transformed from Gaia photometry were corrected based on other sample stars. Moreover, $V$ and $K$ band magnitudes were also computed for the sample stars from Gaia photometry. All the photometric magnitudes under consideration are listed in Table 2.

Figure 2 shows a color−magnitude diagram (CMD) of Eridanus, where the photometric catalog of Muñoz et al. (2018) is used. Gray dots indicate stars located within the tidal radius of 3.′17 (Myeong et al. 2017). Using grids of PARSEC isochrones to fit the CMD distribution, we determined the age of Eridanus to be $10.0 \pm 0.5$ Gyr and metallicity to be $-1.45 \pm 0.05$ dex. The distance modulus and reddening $E(g-r)$ were also derived as $19.83 \pm 0.04$ and $0.025 \pm 0.010$ mag, respectively. A distance of $92.47 \pm 1.71$ kpc is then obtained based on the distance modulus. Considering the $V$-band magnitude 15.02 mag of Eridanus derived by Baumgardt et al. (2020), the absolute visual magnitude is $M_V = -4.81$ mag. An $E(B-V)$ of $0.021 \pm 0.008$ mag was derived by adopting the extinction coefficients in McCall (2004). These parameters have also been determined in previous studies. For example, the metallicity of $-1.35 \pm 0.2$ dex, a distance of 81 kpc to the Sun and an absolute visual magnitude of −4.85 mag have been derived by Da Costa (1985) via CMD fitting for the first time. The distance of 90.1 kpc to the Sun by Stetson et al. (1999) and the metallicity of −1.43, which is the average of the values by Armandroff & Da Costa (1991) and Carretta et al. (2009), are adopted by Harris (1996, 2010 edition) in the GC catalog. Baumgardt & Vasiliev (2021) derived a distance of 84.68 kpc. An absolute age of 10.5 Gyr was obtained by Beccari et al. (2012) for this GC. For $E(B-V)$, a weighted average value of 0.02 mag considering several sources is adopted by Harris (1996, 2010 edition), and Muñoz et al. (2018) determined it to be 0.018 mag. We conclude that our results of these parameters are consistent with those of previous works.

The stars that we observed are shown in Figure 2 with large colored symbols. There are two asymptotic giant branch (AGB) stars, 12 red giant branch (RGB) stars[14], and five horizontal-branch (HB) stars (Table 2). We checked their proper motions from Gaia DR2 (Gaia Collaboration et al. 2018) as shown in Figure 3. All the HB stars and the faintest three RGB stars (represented by solid triangles in Figures 2 and 3) have much larger uncertainties in their proper motions, compared with those brighter RGB and AGB stars (represented by solid circles). Since the G magnitudes of the fainter ones in our sample are about 20–21 mag, their uncertainties are comparable to the documented typical values (1.2–3 mas yr$^{-1}$) at this magnitude range (Gaia Collaboration et al. 2018).

### 3.2. Stellar Parameters

The effective temperature ($T_{\rm eff}$) was first determined based on Gaia photometry, considering the color−temperature relations provided in Mucciarelli & Bellazzini (2020). Six relatively independent determinations of $T_{\rm eff}$ were computed based on the de-reddened colors of $(BP-RP)$, $(BP-G)$, $(G-RP)$, $(BP-K)$, $(RP-K)$, and $(G-K)$. Converting the de-reddened $(g-r)$ color into the color $(B-V)$ adopting the transformation provided by Jester et al. (2005), we also considered another group of $T_{\rm eff}$ based on the color $(B-V)$, which was derived using the color−temperature relation provided in González Hernández & Bonifacio (2009). The final $T_{\rm eff}$ was determined as the mean value of all the above seven values of $T_{\rm eff}$ after a sigma clipping. The associated errors were estimated taking the dispersions of the photometric calibrations and the uncertainties in the color index and [Fe/H] into account. We estimated the stellar masses based on the

[13] https://gea.esac.esa.int/archive/documentation/GDR2/Data_processing/chap_cu5pho/sec_cu5pho_calibr/ssec_cu5pho_PhotTransf.html

[14] For two of these stars, it is difficult to distinguish between RGB or AGB based on their positions in CMD, but in our study, we take them to be RGB stars.

**Table 2**
Basic Information on the Sample of Stars

| ID | R.A. (J2000) | Decl. (J2000) | $G$ (mag) | e_G (mag) | BP (mag) | e_BP (mag) | RP (mag) | e_RP (mag) | $g$ (mag) | e_g (mag) | $r$ (mag) | e_r (mag) | pmRA (mas yr$^{-1}$) | e_pmRA (mas yr$^{-1}$) | pmDec (mas yr$^{-1}$) | e_pmDec (mas yr$^{-1}$) | Evol. Phase |
|---|---|---|---|---|---|---|---|---|---|---|---|---|---|---|---|---|---|
| eri01 | 66.176910 | −21.167276 | 19.650 | 0.005 | 19.992 | 0.054 | 18.885 | 0.030 | 20.215 | 0.003 | 19.560 | 0.003 | 1.1810 | 0.6248 | −0.8417 | 0.6942 | RGB |
| eri02 | 66.168472 | −21.170403 | 20.322 | 0.007 | 20.602 | 0.083 | 19.694 | 0.047 | 20.809 | 0.004 | 20.194 | 0.003 | −0.0457 | 1.0429 | 1.4722 | 1.2958 | RGB |
| eri03 | 66.182945 | −21.174185 | 18.013 | 0.002 | 18.687 | 0.018 | 17.251 | 0.009 | 18.872 | 0.002 | 17.946 | 0.002 | 0.7988 | 0.2064 | −0.1627 | 0.2227 | RGB |
| eri04 | 66.185150 | −21.175451 | 18.340 | 0.002 | 18.994 | 0.025 | 17.593 | 0.011 | 19.125 | 0.002 | 18.267 | 0.002 | 0.3653 | 0.2587 | −0.9767 | 0.2822 | RGB |
| eri05 | 66.173363 | −21.179552 | 18.407 | 0.002 | 18.984 | 0.021 | 17.652 | 0.014 | 19.178 | 0.002 | 18.332 | 0.002 | 0.5388 | 0.2920 | −0.4840 | 0.3129 | RGB |
| eri06 | 66.194931 | −21.180887 | 19.862 | 0.005 | 20.070 | 0.048 | 19.231 | 0.062 | 20.263 | 0.003 | 19.782 | 0.003 | −0.5298 | 0.8228 | 0.4895 | 0.7989 | HB |
| eri07 | 66.184982 | −21.181849 | 18.773 | 0.003 | 19.252 | 0.028 | 18.107 | 0.020 | 19.390 | 0.002 | 18.696 | 0.002 | 0.7575 | 0.3397 | −0.5467 | 0.3856 | AGB |
| eri08 | 66.183861 | −21.183519 | 17.328 | 0.002 | 17.876 | 0.012 | 16.388 | 0.006 | 18.309 | 0.000 | 17.248 | 0.000 | 0.4355 | 0.1299 | −0.1746 | 0.1437 | RGB |
| eri09 | 66.181190 | −21.184744 | 18.068 | 0.002 | 18.680 | 0.020 | 17.290 | 0.009 | 18.895 | 0.002 | 17.999 | 0.002 | 0.7367 | 0.2031 | −1.0208 | 0.2285 | RGB |
| eri10 | 66.187309 | −21.185621 | 17.073 | 0.002 | 17.835 | 0.010 | 16.203 | 0.005 | 18.210 | 0.000 | 17.020 | 0.000 | 0.4044 | 0.1173 | −0.5422 | 0.1333 | RGB |
| eri11 | 66.188339 | −21.188213 | 19.143 | 0.003 | 19.450 | 0.035 | 18.369 | 0.025 | 19.691 | 0.003 | 19.050 | 0.003 | 0.5976 | 0.4182 | −0.9497 | 0.4862 | AGB |
| eri12 | 66.195686 | −21.189545 | 20.644 | 0.008 | 20.757 | 0.122 | 19.920 | 0.090 | 21.113 | 0.004 | 20.531 | 0.004 | 3.4233 | 1.5259 | −0.2365 | 1.3503 | RGB |
| eri13 | 66.185699 | −21.190716 | 20.558 | 0.009 | 20.512 | 0.082 | 19.853 | 0.095 | 20.997 | 0.005 | 20.415 | 0.004 | −0.2745 | 1.3342 | 2.3632 | 1.5846 | RGB |
| eri14 | 66.182388 | −21.191929 | 20.171 | 0.007 | 20.453 | 0.070 | 19.597 | 0.057 | 20.500 | 0.004 | 20.080 | 0.003 | 0.5595 | 0.9482 | −1.7182 | 1.2901 | HB |
| eri15 | 66.185364 | −21.195387 | 18.719 | 0.003 | 19.251 | 0.020 | 18.016 | 0.015 | 19.426 | 0.002 | 18.637 | 0.002 | 0.8461 | 0.3807 | −0.6992 | 0.3909 | RGB |
| eri16 | 66.186218 | −21.197334 | 20.149 | 0.006 | 20.312 | 0.050 | 19.496 | 0.038 | 20.493 | 0.003 | 20.081 | 0.003 | 0.0457 | 0.9189 | 2.1428 | 1.0991 | HB |
| eri17 | 66.177940 | −21.202587 | 18.988 | 0.003 | 19.528 | 0.025 | 18.262 | 0.019 | 19.642 | 0.002 | 18.903 | 0.002 | 0.3619 | 0.3844 | 0.0074 | 0.4424 | RGB |
| eri18 | 66.172325 | −21.141823 | 20.047 | 0.007 | 20.092 | 0.065 | 19.488 | 0.094 | 20.232 | 0.003 | 19.972 | 0.004 | −1.3608 | 0.6670 | −3.3207 | 0.8347 | HB |
| eri19 | 66.189949 | −21.221462 | 20.678 | 0.010 | 20.901 | 0.103 | 20.239 | 0.115 | 21.012 | 0.004 | 20.581 | 0.005 | 2.8056 | 1.6933 | −2.7386 | 2.0293 | HB |

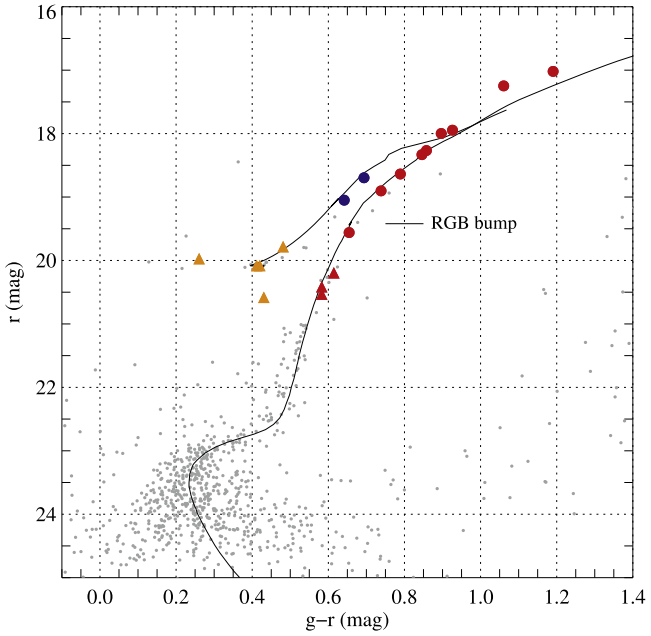


**Figure 2.** CMD of Eridanus. The colors red, blue, and yellow represent the RGB, AGB, and HB stars in our sample, respectively. The solid circles and triangles mark the status of the stellar proper motions (see the text for details). Gray dots represent stars from Muñoz et al. (2018) that are located within the tidal radius of 3′.17 (Myeong et al. 2017). A PARSEC isochrone of the age of 10 Gyr and metallicity of −1.45 is shown, and the position of the RGB bump is also indicated.

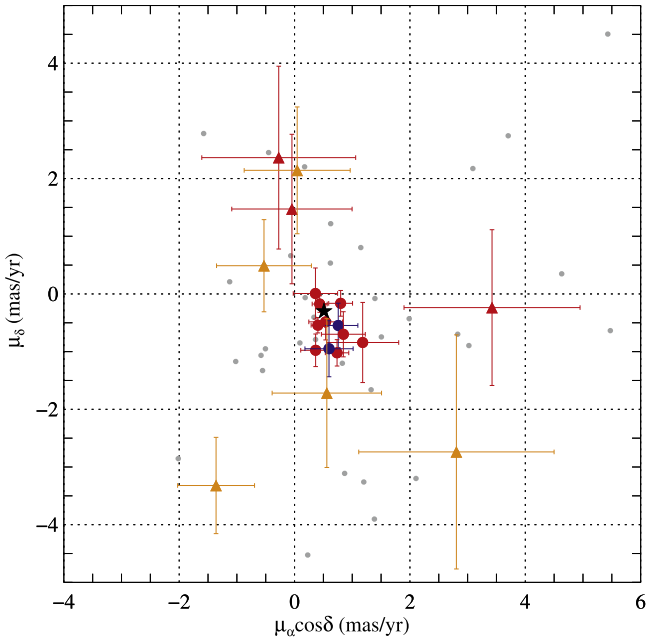


**Figure 3.** Proper motions of our sample stars. The symbols are the same as those in Figure 2 and the size of the error bars indicates the uncertainties in proper motions. Solid triangles represent the HB stars and the faintest three RGB stars, which have much larger errors in their proper motions compared with the brighter RGB and AGB stars, represented by solid circles. Gray dots are part of the background stars shown in Figure 2 that have Gaia DR2 proper motion values. The black star indicates the mean proper motion of Eridanus derived by Vasiliev & Baumgardt (2021).

isochrone (Table 3). Then, the surface gravities ($\log g$) were derived from $T_{\rm eff}$, stellar masses, and bolometric luminosities. The relations of Alonso et al. (1999) were used to calculate the bolometric corrections.

Considering the derived $T_{\rm eff}$ of HB stars and the three faintest RGB stars (represented by solid triangles in Figures 2 and 3) are all above 5500 K, the CN and CH molecular lines are weak for these hot stars; moreover, their uncertainties in proper motions are much larger than other those of brighter stars and their S/Ns are substantially lower, so we opted to neglect these hotter and fainter stars in the following analysis and discussion. In other words, we only consider the brighter RGB and AGB stars as our final sample. The derived $T_{\rm eff}$, $\log g$ and their associated errors for each star in the final sample are listed in Table 3. The typical errors in $T_{\rm eff}$ and $\log g$ are about ±50 K and ±0.03 dex, respectively.

### 3.3. Spectral Indices and Abundances

Following the definition of Harbeck et al. (2003), we computed the spectral indices of CN4142 and CH4300 on the co-added calibrated spectra for each star.

$$\mathrm{CN4142} = -2.5\log\frac{F_{4120-4216}}{0.4F_{4055-4080}+0.6F_{4240-4280}}, \quad (1)$$

$$\mathrm{CH4300} = -2.5\log\frac{F_{4285-4315}}{0.5F_{4240-4280}+0.5F_{4390-4460}}, \quad (2)$$

where $F_{X-Y}$ is the summed spectral flux from $X$ to $Y$ Å. Figure 1 shows the spectral regions used to measure the indices of CN4142 and CH4300. The errors in spectral indices were estimated mainly considering two factors, i.e., the errors of calibrating observed spectra with model spectra and the flux dispersion among calibrated OB spectra. Table 3 lists the derived spectral index values and their errors. Note that we did not plot $\delta$CN versus $\delta$CH (e.g., Gerber et al. 2020) here because we do not have enough stars to define baselines where $\delta\mathrm{CN}=0$ and $\delta\mathrm{CH}=0$.

To analyze [C/Fe] and [N/Fe] specifically, we took advantage of the model spectra from iSpec. For each star, we generated a grid of model spectra with [C/Fe] = −0.8, −0.7, −0.6, ... 0, and [N/Fe] = 0.3, 0.4, 0.5, ... 1.8. [O/Fe] was assumed to be solar for all the model spectra.[15] The model spectral indices of CN4142 and CH4300 were computed for each model spectrum to construct a grid of model spectral indices for each star. By interpolation, we found the best match to the observed spectral indices from the model grid to derive a pair of best-matched [C/Fe] and [N/Fe]. In order to derive more reliable abundances as well as to estimate their errors, we performed the interpolation 1000 times for each star, considering 1$\sigma$ variations in a Gaussian Monte Carlo approach in the input data. The mean abundances and their standard deviations are adopted as the final abundances of [C/Fe] and [N/Fe] and their errors, where the typical errors (median value) are 0.03 and 0.06 dex for [C/Fe] and [N/Fe], respectively. The results of the final sample stars are summarized in Table 3. By examining the dispersions ($\sigma$) and the interquartile range (IQR) values of carbon and nitrogen abundances, which are $\sigma_{\rm [C/Fe]}=0.15$, $\mathrm{IQR}_{\rm [C/Fe]}=0.11$, and $\sigma_{\rm [N/Fe]}=0.16$, $\mathrm{IQR}_{\rm [N/Fe]}=0.20$, respectively, we find that the dispersions of [C/Fe] and [N/Fe] are similar and both significantly larger than their associated errors, while [C/Fe] distributes more concentratedly. These can

[15] According to our test shown in Tang et al. (2021), the difference in the indices for CN4142 and CH4300 caused by an [O/Fe] difference of 0.4 dex is almost negligible inside the temperature range discussed.

**Table 3**
Stellar Parameters, Spectral Indices, and Abundances of the Final Sample of Stars

| ID | Mass ($M_\odot$) | $T_{\rm eff}$ (K) | e_$T_{\rm eff}$ (K) | log $g$ | e_log $g$ | CN4142 | e_CN4142 | CH4300 | e_CH4300 | [C/Fe] | e_[C/Fe] | [N/Fe] | e_[N/Fe] |
|---|---|---|---|---|---|---|---|---|---|---|---|---|---|
| eri01 | 0.847 | 5101 | 106.58 | 2.15 | 0.05 | −0.017 | 0.007 | 0.209 | 0.005 | −0.21 | 0.02 | 1.31 | 0.26 |
| eri03 | 0.836 | 4410 | 35.14 | 1.18 | 0.03 | −0.005 | 0.008 | 0.273 | 0.007 | −0.58 | 0.04 | 1.24 | 0.08 |
| eri04 | 0.839 | 4468 | 37.62 | 1.34 | 0.03 | −0.012 | 0.006 | 0.279 | 0.006 | −0.52 | 0.03 | 1.17 | 0.06 |
| eri05 | 0.840 | 4568 | 38.66 | 1.42 | 0.03 | 0.007 | 0.008 | 0.281 | 0.005 | −0.43 | 0.02 | 1.32 | 0.05 |
| eri07 | 0.780 | 4896 | 47.80 | 1.67 | 0.03 | 0.005 | 0.007 | 0.185 | 0.005 | −0.51 | 0.03 | 1.60 | 0.11 |
| eri08 | 0.828 | 4384 | 55.01 | 0.89 | 0.04 | 0.020 | 0.006 | 0.290 | 0.005 | −0.52 | 0.02 | 1.33 | 0.04 |
| eri09 | 0.837 | 4478 | 32.70 | 1.24 | 0.03 | 0.007 | 0.007 | 0.290 | 0.006 | −0.45 | 0.03 | 1.28 | 0.06 |
| eri10 | 0.819 | 4173 | 42.12 | 0.67 | 0.03 | 0.037 | 0.008 | 0.274 | 0.006 | −0.65 | 0.03 | 1.54 | 0.07 |
| eri11 | 0.790 | 5101 | 83.02 | 1.91 | 0.04 | 0.006 | 0.005 | 0.214 | 0.005 | −0.12 | 0.02 | 1.69 | 0.05 |
| eri15 | 0.842 | 4723 | 36.71 | 1.61 | 0.03 | −0.001 | 0.004 | 0.264 | 0.010 | −0.39 | 0.04 | 1.38 | 0.04 |
| eri17 | 0.844 | 4690 | 38.31 | 1.71 | 0.03 | 0.006 | 0.007 | 0.245 | 0.010 | −0.50 | 0.04 | 1.45 | 0.06 |

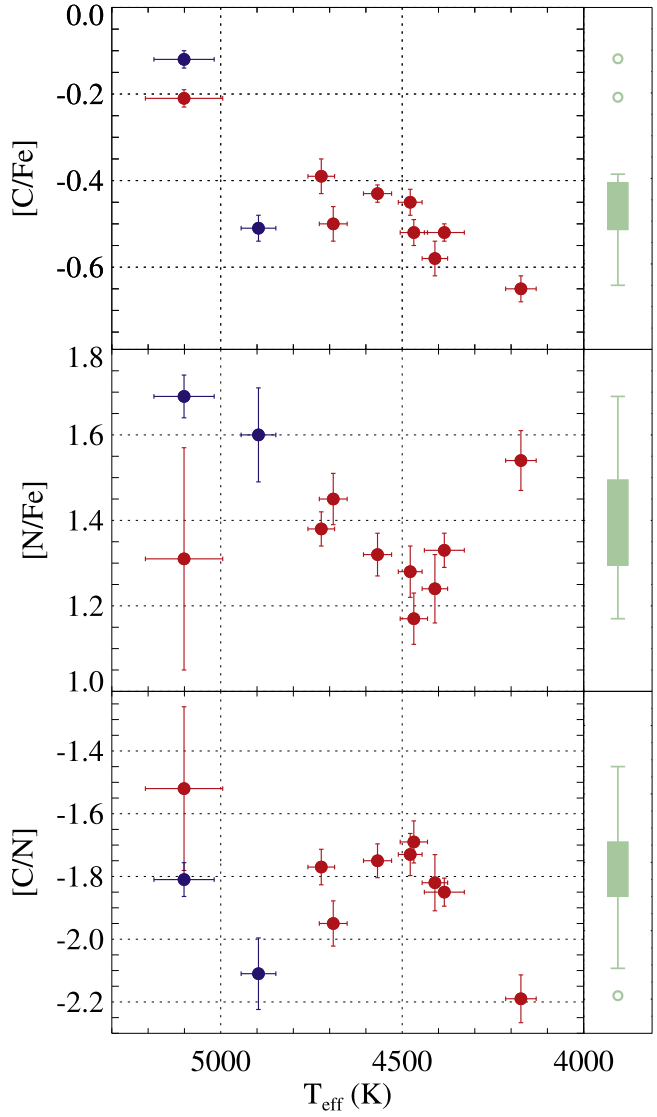


**Figure 4.** Distribution of the abundance ratios of [C/Fe], [N/Fe], and [C/N]. The colors of the symbol are the same as those in Figure 2. A box plot of each distribution of abundance is also shown on the right side of each panel, where the green thick bar indicates the IQR covering the central 50% of the data, the thin lines extending from the thick bar covering the range of the remaining data, while the individual small circles mark the outliers located further than 1.5 times the IQR from the edge of the thick bar.

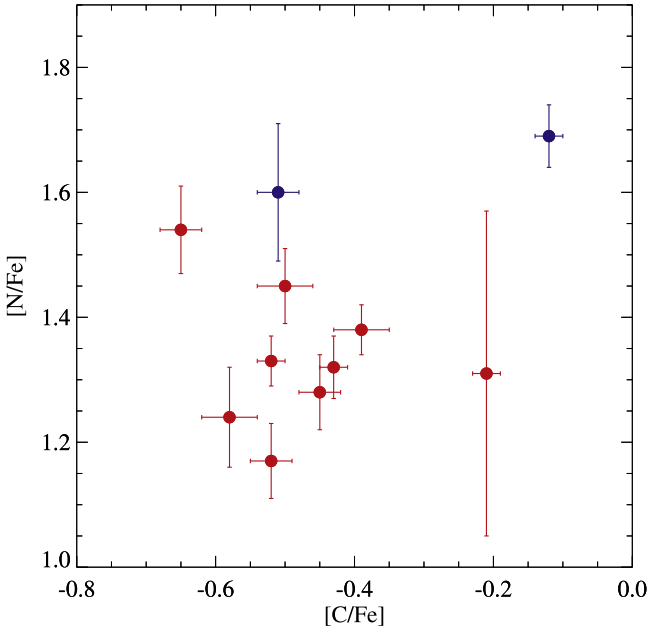


**Figure 5.** [C/Fe] vs. [N/Fe]. Symbols are the same as those in Figure 2.

also be detected visually in Figure 4, which shows the distributions of [C/Fe] and [N/Fe], as well as the [C/N] ratio.

The activated CNO cycle in the cores of evolved low-mass stars may change the surface chemical abundances if the convective envelope reaches deep enough. As stars climb up the RGB, the surface abundances of carbon and nitrogen would become altered due to the first dredge-up and extra-mixing processes. Especially, the extra-mixing process can significantly change the surface abundances of stars brighter than the RGB bump (e.g., Gratton et al. 2000; Charbonnel & Zahn 2007; Lagarde et al. 2012). As shown in Figure 2, only the faintest RGB star in our final sample is located below the RGB bump, while all the others should have experienced the extra mixing. So the distributions of abundance shown in Figure 4 are a mixture of the results of the original chemical composition and their self-evolution. In that sense, the lack of anticorrelation for [C/Fe] versus [N/Fe] (Figure 5) is not surprising. A similar situation can be found for other GCs with a small sample size (e.g., Mészáros et al. 2020).

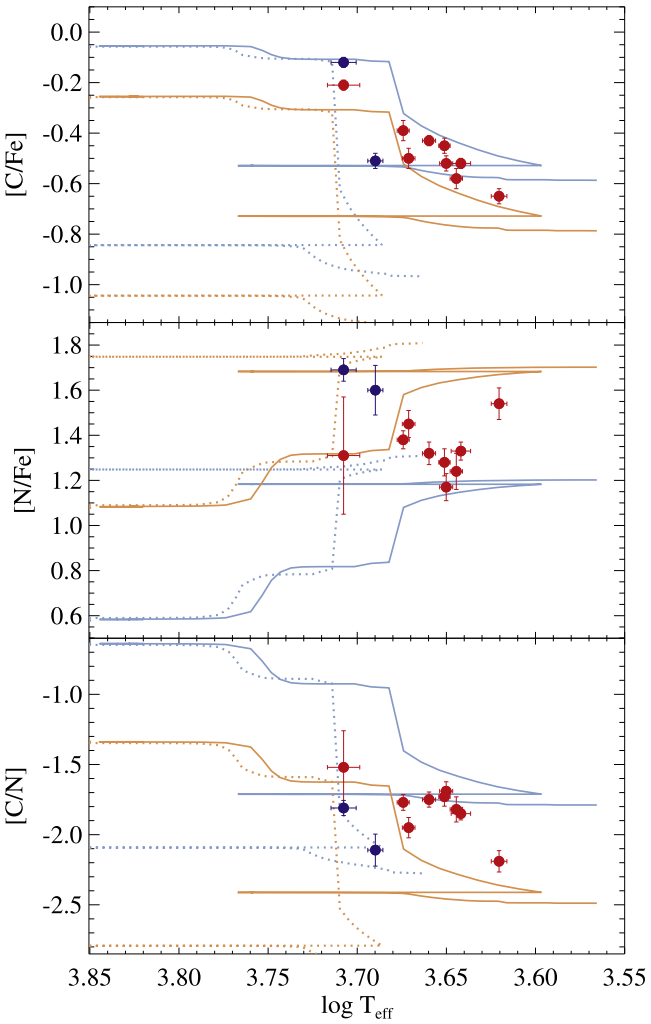


**Figure 6.** Comparison between the distributions of [C/Fe], [N/Fe], [C/N] and the model predictions. Symbols are the same as those in Figure 2. Models including thermohaline convection and rotation-induced mixing from Lagarde et al. (2012) are considered here. Blue and orange lines represent model predictions for the stellar mass of 0.85 $M_{\odot}$ with initial chemical compositions of [C/Fe] = −0.05, [N/Fe] = +0.6, and [C/Fe] = −0.25, [N/Fe] = +1.1, respectively, mimicking the primordial and enriched stellar populations, while solid and dotted lines represent those for metallicities of $Z = 0.002$ and 0.0001 ([Fe/H] = −0.86 and −2.16), respectively.

To investigate the influence of the extra-mixing process in our sample, we took advantage of the models of Lagarde et al. (2012) where thermohaline convection and rotation-induced mixing are included. In parallel with our derived abundances, the model predictions for the stellar mass of 0.85 $M_{\odot}$ are shown in Figure 6, considering the initial chemical compositions of [C/Fe] = −0.05, [N/Fe] = +0.6 (blue lines) and [C/Fe] = −0.25, [N/Fe] = +1.1 (orange lines), mimicking the primordial and enriched stellar populations, respectively. In terms of carbon abundances, the observed data points are well constrained by models with [C/Fe] = −0.25 to −0.05, and the abundance trend with $T_{\rm eff}$ follows the model prediction exactly. This implies that (a) the decrease in carbon abundance with decreasing $T_{\rm eff}$ is obviously a result of stellar evolutionary mixing; (b) the initial carbon abundance spread among our sample stars is around ∼0.2 dex, which is slightly larger than our determination error (∼0.03 dex in average). On the other hand, the surface abundance of nitrogen is expected to increase as a result of extra mixing, but the observed values do not follow the predictions of models with a single or a narrow range of initial [N/Fe]. Clearly, multiple models with initial [N/Fe] between +0.6 and +1.1 are needed to cover our data points. A difference of 0.5 dex in [N/Fe] is no doubt larger than the observed abundance errors (∼0.08 dex on average). Moreover, a scatter of about 0.7 dex in [C/N] can also be deduced, which is also significant compared with the average error of ∼0.06 dex. Therefore, the existence of variations in abundance among our observed member stars is suggested by (1) the apparent distributions of abundance with no evolutionary effect considered (Figure 4) and (2) the stellar evolutionary models considering the extra-mixing processes of Lagarde et al. (2012) (Figure 6). In conclusion, we find clear evidence that indicates the existence of MPs in GC Eridanus, particularly in nitrogen abundances.

## 4. Discussion

### 4.1. Eridanus

Given its higher metallicity ([Fe/H] ∼ −1.4) compared to other outer halo GCs, and slightly younger age (10.5 Gyr), Eridanus is considered to have formed ex situ. Carballo-Bello et al. (2015) speculated that Eridanus may be related to the Monoceros Ring since this GC lies in its predicted orbit. However, recent studies showed that the Monoceros Ring is part of the outer Galactic disk with Galactocentric distances <30 kpc (Li et al. 2021), and therefore their connection seems unlikely. On the other hand, Myeong et al. (2017) discovered two symmetrical tidal tails around Eridanus using *g*- and *i*-band deep imaging, which span about 760 pc in length. According to the great circle generated along the direction of the tidal tails, they instead suggested that Eridanus could have a possible association with one of the four dwarf galaxies: Sculptor, Canes Venatici I, Canes Venatici II, or Fornax, of which Sculptor has a distance similar to that of Eridanus. The discovery of symmetrical, long tidal tails around Eridanus indicates that it has gone through a significant mass-loss phase. This has two implications: (1) the initial mass should be much higher than the current mass, and thus our discovery of MPs in this GC does not necessarily contradict the current MP scenarios. A similar situation was found in Pal 13 (Tang et al. 2021); (2) Eridanus could have undergone stripping due to a radial orbit, causing stars to drift away from the Lagrange points of the cluster. However, its connection with low-mass dwarf galaxies, e.g., Sculptor, may cause a logical dilemma. The existence of Eridanus is at odds with the lack of an existing GC in Sculptor, and our discovery of N-enhanced stars in Eridanus is inconsistent with the null detection of N-rich field stars in Sculptor (Lardo et al. 2016; Tang et al. 2022). Therefore, their association is less likely from a chemical point of view. Massari et al. (2019) analyzed the origins of Galactic clusters by combining kinematic information and available cluster ages, where Eridanus is suggested to have been accreted from a low-mass progenitor. There are still many unanswered questions regarding its origin, evolution, composition, etc. The upcoming China Space Station Telescope (CSST) will give us a more complete picture of Eridanus by (1) exploring its tidal tail mass with deep photometry and (2) investigating its cluster mass function and MPs on the main sequence with UV-optical filters.

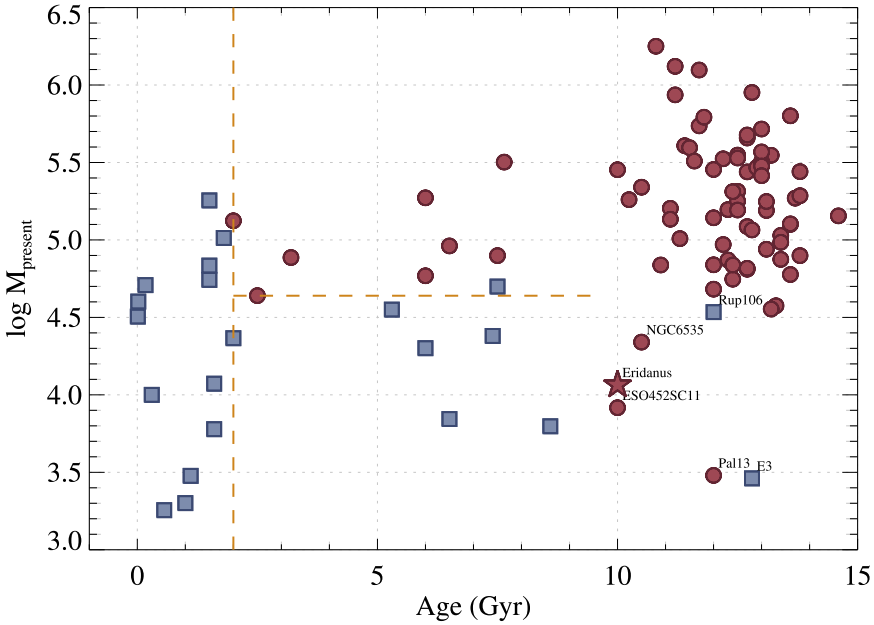


**Figure 7.** Age–present mass plane for clusters with (red circles) and without (blue squares) MPs. Eridanus is represented by a red star. The orange-dashed lines indicate the rough separation in age and mass between clusters with and without MPs.

### *4.2. Threshold Mass for the Formation of MPs*

The distribution of age versus present-day mass for clusters with and without MPs was initially presented by Martocchia et al. (2018), where the data of the compilation by Krause et al. (2016) was considered. We further add data points from recent works, e.g., Salinas & Strader (2015), Niederhofer et al. (2017a, 2017b), Simpson et al. (2017), Tang et al. (2017), Hollyhead et al. (2018), Zhang et al. (2018), Li & de Grijs (2019), Li et al. (2019, 2020), Milone et al. (2020), Tang et al. (2021), Fernández-Trincado et al. (2022), as well as this work (Figure 7). We take the masses of the Milky Way GCs from the most recent version of the Galactic Globular Cluster Database from Baumgardt & Hilker (2018), which has been updated to include the Gaia EDR3 data. We also include data for several large clusters from the Large and Small Magellanic Clouds (LMC/SMC). The ages of the clusters have been taken from recent literature while their present-day masses are calculated by fitting *N*-body models to archival Hubble Space Telescope photometry, similar to what Baumgardt & Hilker (2018) did for Galactic GCs. The initial masses for these clusters are calculated by using the present-day masses and applying the models of Baumgardt et al. (2013).

As previously suggested, the separation of clusters with and without MPs at the age of ∼2 Gyr can be clearly seen in the figure. For clusters younger than 10 Gyr, those with masses under $\log M \sim 4.65$ do not show MPs. However, this condition is ambiguous for GCs over 10 Gyr, since several low-mass GCs, e.g., NGC 6535 (Bragaglia et al. 2017), Eridanus (this work, represented by a red star), ESO452-SC11 (Simpson et al. 2017), and Pal 13 (Tang et al. 2021), also possess MPs. According to the updated mass estimation, Pal 13 is the lowest-mass cluster with MP signals. The studies of old, low-mass GCs play a key role in revealing the formation and evolution of MPs.

During the long time self-evolution and coevolution with the Milky Way, old GCs may experience complex mass loss. If a GC has an initial mass high enough to form MPs, and then loses a large amount of its mass during its long time evolution, it can become an old, low-mass GC showing MPs. In this context, the information on cluster initial masses is fundamental to understanding the formation of MPs (e.g., Carretta et al. 2010; Milone et al. 2020). Baumgardt et al. (2019) computed the initial masses for Galactic GCs using an *N*-body simulation, while those of clusters in LMC/SMC will be presented in a forthcoming paper. In Figure 8 we present the age–initial mass distribution of the cluster sample, where the LMC/SMC clusters without known initial masses are excluded. We find that the dispersion in initial cluster masses is smaller compared to that of their present-day masses, and most old (age $\geqslant$ 10 Gyr) GCs with MPs have initial masses above $\log M_{\rm initial} \sim 5.2$. Two of the aforementioned old low-mass GCs, NGC 6535 and ESO452-SC11, have initial masses as high as most of the other old GCs, and thus their MPs can be easily explained. For Eridanus and Pal 13, considering their probable external origins, their real initial masses could be higher, since Baumgardt et al. (2019) only considered the GC orbits within the Milky Way in the simulation, and the mass loss before and during their merger into the Milky Way have been omitted.

Considering the uncertainties in the initial mass estimation for accreted clusters, in situ ones can provide a simpler sample for analyzing the cluster mass threshold for the formation of MPs. We divide the Galactic GCs into in situ ones and accreted ones, according to the category in Massari et al. (2019). Clusters in LMC and SMC are treated as in situ ones (Figure 8). In the in situ sample, there is a slight trend in the clusters with MPs (older than ∼2 Gyr) that the older they are, the higher initial masses they have. Among them, NGC 6838 has the lowest initial mass of $\log M_{\rm initial} \sim 5.26$ at the old cluster end, while at the young cluster end, Hodge 6 has the lowest initial mass of $\log M_{\rm initial} \sim 4.98$. This may give a rough initial mass threshold, if it exists, for clusters to form MPs. However, more observations of old in situ GCs with low initial masses, e.g., Pal 1 and Pal 11, are still necessary before drawing any firm conclusion.

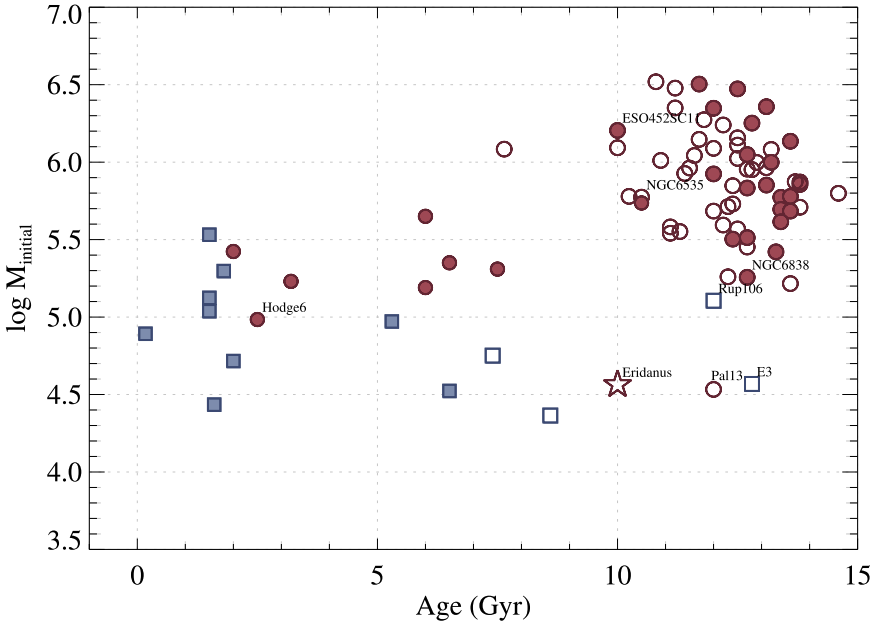


**Figure 8.** Age–initial mass plane for clusters with and without MPs. The symbol shapes and colors are the same as those in Figure 7. The origins of the clusters are indicated according to Massari et al. (2019), where solid symbols represent in situ clusters, and open ones represent accreted clusters

## 5. Summary

Mass has been generally considered one of the key parameters in determining whether a stellar cluster will have MPs or not. In order to explore the possible mass threshold for the formation of MPs, we studied the composition of the stellar population in low-mass GCs. In this work, we focus on the GC Eridanus, with a present-day mass of $1.16 \times 10^4\,M_{\odot}$ (Baumgardt et al. 2019).

Based on its CMD, we determined the age, metallicity, distance modulus, and distance for Eridanus, which are $10.0 \pm 0.5$ Gyr, $-1.45 \pm 0.05$ dex, $19.83 \pm 0.04$ mag, and $92.47 \pm 1.71$ kpc, respectively. These are consistent with the values derived in previous studies.

In order to investigate whether MPs exist in Eridanus, blue-UV low-resolution spectra were obtained with OSIRIS/MOS on board GTC for 19 member stars to study their carbon and nitrogen abundances. After determining their effective temperature and surface gravity photometrically, the spectral indices of CH4300 and CN4142 were computed for the final sample, including nine RGB stars and two AGB stars. Then, with the help of model spectra, we derived the values of [C/Fe] and [N/Fe] for these stars. Since most of them have evolved past the RGB bump, where extra mixing may significantly alter their surface chemical composition, we compared the observed abundances with stellar evolutionary models considering thermohaline instability and rotation-induced mixing. We find that besides the variations in carbon and nitrogen abundances caused by stellar evolution, the imprint of initial elemental abundance dispersion is prominently present in the observed distribution of nitrogen abundance, which indicates the existence of MPs in Eridanus.

To find further investigate the critical cluster mass for MPs, we updated the age–mass distribution plane for all clusters that have been studied for MPs. Although a threshold of present-day mass at $\log M \sim 4.65$ seems to exist for clusters younger than 10 Gyr, the condition for GCs older than 10 Gyr is unclear. Taking the mass loss during the long time evolution of GCs into consideration, the initial mass of clusters should be a more reasonable parameter to analyze when studying the formation of MPs. We then constructed the age–initial mass plane with clusters in the Milky Way and LMC/SMC. To avoid the influence of the uncertainty in the initial mass estimation of accreted clusters, we simplified our sample with only in situ clusters.[16] Then, a slight trend of initial mass increases with increasing age is found for clusters (older than 2 Gyr) with MPs, and $\log M_{\rm initial} \sim 4.98$ and 5.26 are the lowest initial mass at the young and old ends, respectively, which might provide a reference for the critical mass for clusters to form MPs.

However, current observations are still incomplete for a study on this topic. Other low initial mass in situ clusters must still be studied before we are able to have a comprehensive understanding. In this context, the upcoming space telescopes, e.g., the CSST, as well as the ground-based next-generation large telescopes, e.g., the Thirty Meter Telescope and Extremely Large Telescope, will provide exciting opportunities for observations and studies in this field.

Y.W. acknowledges the support of the National Natural Science Foundation of China under grant No. 11803048 and the Special Research Assistant Foundation Project of the Chinese Academy of Sciences. B.T. was supported by the Natural Science Foundation of Guangdong Province under grant No. 2022A1515010732 and the National Natural Science Foundation of China under grant No. U1931102. C.L. was supported by the National Natural Science Foundation of China through grant Nos. 12037090 and 11803048, Guangdong Major Project of Basic and Applied Basic Research (grant No. 2019B030302001), and the Hundred Talents Program of Sun Yat-sen University. Y.W., B.T., and C.L. acknowledge the support of the National Natural Science Foundation of China through grant No. 12233013, and from the China Manned

[16] We note that theoretically one does not expect the formation of MPs to depend on whether or not the cluster was formed in situ or not.

Space Project through the science research grant Nos. CMS-CSST-2021-A08 and CMS-CSST-2021-B03. R.R.M. gratefully acknowledges the support from the ANID BASAL under project No. FB210003. J.G.F.-T. gratefully acknowledges the grant support provided by Proyecto Fondecyt Iniciación No. 11220340, and also from ANID Concurso de Fomento a la Vinculación Internacional para Instituciones de Investigación Regionales (Modalidad Corta Duración) Proyecto No. FOVI210020, and from the Joint Committee ESO-Government of Chile 2021 (ORP 023/2021). D.G. gratefully acknowledges support from the ANID BASAL project ACE210002. D.G. also acknowledges financial support from the Dirección de Investigación y Desarrollo de la Universidad de La Serena through the Programa de Incentivo a la Investigación de Académicos (PIA-DIDULS). This work is based on observations made with the Gran Telescopio Canarias (GTC), installed in the Spanish Observatorio del Roque de los Muchachos of the Instituto de Astrofisica de Canarias, on the island of La Palma. This work uses the data obtained from the European Space Agency (ESA) space mission Gaia.

## ORCID iDs

Yue Wang https://orcid.org/0000-0002-7531-603X
Baitian Tang https://orcid.org/0000-0002-0066-0346
Chengyuan Li https://orcid.org/0000-0002-3084-5157
Holger Baumgardt https://orcid.org/0000-0002-1959-6946
Doug Geisler https://orcid.org/0000-0002-3900-8208

## References

Alonso, A., Arribas, S., & Martínez-Roger, C. 1999, A&AS, 140, 261
Armandroff, T. E., & Da Costa, G. S. 1991, AJ, 101, 1329
Asplund, M., Grevesse, N., & Sauval, A. J. 2005, in ASP Conf. Ser. 336, Cosmic Abundances as Records of Stellar Evolution and Nucleosynthesis, ed. I. Barnes, G. Thomas, & F. N. Bash (San Francisco, CA: ASP), 25
Bastian, N., & Lardo, C. 2018, ARA&A, 56, 83
Baumgardt, H., & Hilker, M. 2018, MNRAS, 478, 1520
Baumgardt, H., Hilker, M., Sollima, A., & Bellini, A. 2019, MNRAS, 482, 5138
Baumgardt, H., Parmentier, G., Anders, P., & Grebel, E. K. 2013, MNRAS, 430, 676
Baumgardt, H., Sollima, A., & Hilker, M. 2020, PASA, 37, e046
Baumgardt, H., & Vasiliev, E. 2021, MNRAS, 505, 5957
Beccari, G., Lützgendorf, N., Olczak, C., et al. 2012, ApJ, 754, 108
Bekki, K. 2011, MNRAS, 412, 2241
Blanco-Cuaresma, S. 2019, MNRAS, 486, 2075
Blanco-Cuaresma, S., Soubiran, C., Heiter, U., & Jofré, P. 2014, A&A, 569, A111
Bragaglia, A., Carretta, E., D'Orazi, V., et al. 2017, A&A, 607, A44
Carballo-Bello, J. A., Muñoz, R. R., Carlin, J. L., et al. 2015, ApJ, 805, 51
Carretta, E., Bragaglia, A., Gratton, R., D'Orazi, V., & Lucatello, S. 2009, A&A, 508, 695
Carretta, E., Bragaglia, A., Gratton, R. G., et al. 2010, A&A, 516, A55
Cesarsky, D. A., Laustsen, S., Lequeux, J., Schuster, H. E., & West, R. M. 1977, A&A, 61, L31
Charbonnel, C., & Zahn, J. P. 2007, A&A, 467, L15
Charlie, C., & Spergel, D. N. 2011, ApJ, 726, 36
Da Costa, G. S. 1985, ApJ, 291, 230
de Mink, S. E., Pols, O. R., Langer, N., & Izzard, R. G. 2009, A&A, 507, L1
Decressin, T., Charbonnel, C., & Meynet, G. 2007a, A&A, 475, 859
Decressin, T., Meynet, G., Charbonnel, C., Prantzos, N., & Ekström, S. 2007b, A&A, 464, 1029
Denissenkov, P. A., & Hartwick, F. D. A. 2014, MNRAS, 437, L21
Denissenkov, P. A., VandenBerg, D. A., Hartwick, F. D. A., et al. 2015, MNRAS, 448, 3314
D'Ercole, A., D'Antona, F., Ventura, P., Vesperini, E., & McMillan, S. L. W. 2010, MNRAS, 407, 854
Fernández-Trincado, J. G., Villanova, S., Geisler, D., et al. 2022, A&A, 658, A116
Gaia Collaboration, Brown, A. G. A., Vallenari, A., et al. 2018, A&A, 616, A1
Gaia Collaboration, Prusti, T., de Bruijne, J. H. J., et al. 2016, A&A, 595, A1
Gerber, J. M., Friel, E. D., & Vesperini, E. 2020, AJ, 159, 50
González Hernández, J. I., & Bonifacio, P. 2009, A&A, 497, 497
Gratton, R., Sneden, C., & Carretta, E. 2004, ARA&A, 42, 385
Gratton, R. G., Sneden, C., Carretta, E., & Bragaglia, A. 2000, A&A, 354, 169
Gustafsson, B., Edvardsson, B., Eriksson, K., et al. 2008, A&A, 486, 951
Harbeck, D., Smith, G. H., & Grebel, E. K. 2003, AJ, 125, 197
Harris, W. E. 1996, AJ, 112, 1487
Hollyhead, K., Lardo, C., Kacharov, N., et al. 2018, MNRAS, 476, 114
Jester, S., Schneider, D. P., Richards, G. T., et al. 2005, AJ, 130, 873
Krause, M. G. H., Charbonnel, C., Bastian, N., & Diehl, R. 2016, A&A, 587, A53
Lagarde, N., Decressin, T., Charbonnel, C., et al. 2012, A&A, 543, A108
Lardo, C., Battaglia, G., Pancino, E., et al. 2016, A&A, 585, A70
Li, C., & de Grijs, R. 2019, ApJ, 876, 94
Li, C., Wang, Y., & Milone, A. P. 2019, ApJ, 884, 17
Li, C., Wang, Y., Tang, B., et al. 2020, ApJ, 893, 17
Li, J., Xue, X.-X., Liu, C., et al. 2021, ApJ, 910, 46
Martocchia, S., Cabrera-Ziri, I., Lardo, C., et al. 2018, MNRAS, 473, 2688
Massari, D., Koppelman, H. H., & Helmi, A. 2019, A&A, 630, L4
Masseron, T., García-Hernández, D. A., Mészáros, S., et al. 2019, A&A, 622, A191
McCall, M. L. 2004, AJ, 128, 2144
Mészáros, S., Masseron, T., García-Hernández, D. A., et al. 2020, MNRAS, 492, 1641
Milone, A. P., & Marino, A. F. 2022, Univ, 8, 359
Milone, A. P., Marino, A. F., Da Costa, G. S., et al. 2020, MNRAS, 491, 515
Milone, A. P., Piotto, G., Renzini, A., et al. 2017, MNRAS, 464, 3636
Mucciarelli, A., & Bellazzini, M. 2020, RNAAS, 4, 52
Muñoz, R. R., Côté, P., Santana, F. A., et al. 2018, ApJ, 860, 65
Myeong, G. C., Jerjen, H., Mackey, D., & Da Costa, G. S. 2017, ApJL, 840, L25
Niederhofer, F., Bastian, N., Kozhurina-Platais, V., et al. 2017a, MNRAS, 464, 94
Niederhofer, F., Bastian, N., Kozhurina-Platais, V., et al. 2017b, MNRAS, 465, 4159
Osborn, W. 1971, Obs, 91, 223
Pancino, E., Rejkuba, M., Zoccali, M., & Carrera, R. 2010, A&A, 524, A44
Pancino, E., Romano, D., Tang, B., et al. 2017, A&A, 601, A112
Piotto, G., Milone, A. P., Anderson, J., et al. 2012, ApJ, 760, 39
Piotto, G., Milone, A. P., Bedin, L. R., et al. 2015, AJ, 149, 91
Renzini, A., D'Antona, F., Cassisi, S., et al. 2015, MNRAS, 454, 4197
Salinas, R., & Strader, J. 2015, ApJ, 809, 169
Simpson, J. D., De Silva, G., Martell, S. L., Navin, C. A., & Zucker, D. B. 2017, MNRAS, 472, 2856
Stetson, P. B., Bolte, M., Harris, W. E., et al. 1999, AJ, 117, 247
Tang, B., Cohen, R. E., Geisler, D., et al. 2017, MNRAS, 465, 19
Tang, B., Wang, Y., Huang, R., et al. 2021, ApJ, 908, 220
Tang, B., Zhang, J., Yan, Z., et al. 2022, arXiv:2210.06731
Vasiliev, E., & Baumgardt, H. 2021, MNRAS, 505, 5978
Ventura, P., & D'Antona, F. 2011, MNRAS, 410, 2760
Vesperini, E., McMillan, S. L. W., D'Antona, F., & D'Ercole, A. 2010, ApJL, 718, L112
Wang, L., Kroupa, P., Takahashi, K., & Jerabkova, T. 2020, MNRAS, 491, 440
Zhang, H., de Grijs, R., Li, C., & Wu, X. 2018, ApJ, 853, 186